FULL RESEARCH ARTICLE

Electron-optical in-situ crack monitoring during electron beam powder bed fusion of the Ni-Base superalloy CMSX-4

Johannes Bäreis[1,2] · Nick Semjatov[1,2] · Jakob Renner[2] · Jihui Ye[1,2] · Fu Zongwen[1,2] · Carolin Körner[1,2]

Abstract

Electron beam powder bed fusion (PBF-EB) of Ni-base superalloys such as CMSX-4 is a demanding process. Using conventional PBF-EB machines, process observation is done by mounting optical camera systems on viewing windows at the top of the build chamber. However, the concomitant metallization blocks optical observation methods with increasing build time. Therefore, build quality evaluation is normally done after the process utilizing visual inspection or subsequent metallurgical analysis. In this work, CMSX-4 is processed using a freely programmable PBF-EB machine with an electron optical (ELO) imaging system. It consists of a four-segment ELO detector and in-house developed imaging software. The ELO system works reliably for almost 30 h of build time and allows a layerwise monitoring of the build area. A comparison of in-situ ELO monitoring and the sample surfaces shows remarkable accordance. Furthermore, ELO imaging is applied to exemplarily document surface cracking over long build times. Therefore, the present study successfully demonstrates the application of ELO imaging for improved process control under the demanding test conditions of Ni-base superalloys.

Keywords Additive manufacturing · Electron-beam powder bed fusion · CMSX-4 · In-situ process monitoring · ELO-imaging

1 Introduction

Electron beam powder bed fusion (PBF-EB) belongs to the powder bed-based group of additive manufacturing (AM) technology. Using an electron beam as the heat source offers significant advantages compared to similar AM technologies, such as selective laser melting (PBF-LM). Unlike in PBF-LM, beam deflection is not done using mechanical mirrors but electromagnetic coils [1]. The beam deflection is, therefore, almost inertia-free and allows velocities of up to 10^5 m/s on the building area. Furthermore, the electron beam can be quickly focused or defocused to control the energy input into the powder bed. This allows the development of novel process strategies for demanding materials, such as Ni-base superalloys [2].

CMSX-4 is a second generation Ni-base superalloy which was originally designed for the casting of components for high-temperature applications, such as turbine blades [3]. Nevertheless, gas-atomized powder composed of CMSX-4 has also been successfully processed into dense cuboidel or cylindrical samples with diameters in range of 12–23 mm and heights of up to 80 mm. The resulting microstructure varies up to single-crystalline samples depending on the applied process strategy. [4–7].

In general, enhanced in-process monitoring has the potential to further establish powder bed-based AM of Ni-base materials thanks to the improved process controlability as well as understanding of defect generation [8]. Conventional PBF-EB machines only offer optical process observation (i.e., IR-cameras) through viewing windows. However, these viewing windows become darkened by metallization over the course of a build experiment. The source of metallization is the evaporation of volatile elements from the generated melt pool [9]. Either mechanical shutters [10] or a rolling

✉ Johannes Bäreis
  johannes.jb.baereis@fau.de

✉ Nick Semjatov
  nick.semjatov@fau.de

1   Joint Institute of Advanced Materials and Processes, University of Erlangen-Nürnberg, Dr.-Mack-Str. 81, 90762 Fürth, Germany

2   Department of Material Science and Engineering, Chair of Materials Science and Engineering for Metals, University of Erlangen-Nürnberg, Martensstr. 5, 91058 Erlangen, Germany

film [11, 12] in front of the viewing windows have been suggested by literature as remedial measures.

Arnold et al. demonstrated electron-optical (ELO) imaging as a robust alternative for process observation during PBF-EB. Similar to scanning electron microscopy, backscattered electrons (BSE) are detected for in-situ imaging of the build area [9]. Its versatility for in-situ quality control during PBF-EB has been shown by different researchers, i.e., for fast process window development by Pobel et al. [13], validation of melt pool simulations by Breuning et al. [14], in-operando monitoring of the melting and dimensional accuracy by Arnold et al. [15, 16], for an arbitrary geometry with complex features by Ledford et al. [17] or off-axially arranged dual-detector ELO-imaging by Zhao et al. [18]. Wong et al. even modified the heat shields of a commercial PBF-EB-machine for ELO-imaging [19]. An overview of the expanding research field of in-situ monitoring is given by Grasso et al. in a recently published review paper [20].

This work exemplifies ELO monitoring during PBF-EB under the demanding process environment of the Ni-base superalloy CMSX-4. A freely programmable PBF-EB machine was combined with an integrated four-segment ELO detector and in-house developed imaging software to monitor the topography and sample cracking. Different imaging modes were compared to the corresponding sample surfaces and the robustness of the system was utilized for monitoring surface cracking over the entire build time.

2 Materials and methods

For the experimental part, a freely programmable PBF-EB system "Freemelt ONE" (FM1, Freemelt AB, Mölndal, Schweden) operating at 60 kV acceleration voltage and up to 6 kW of electron beam power was utilized [21, 22]. The conducted calibration of the FM1 system resulted in a minimum beam diameter of 250 μm FWHP (= Full Width Half Power). The used CMSX-4 powder was argon gas-atomized (TLS Technik GmbH & Co. Spezialpulver KG, Bitterfeld, Germany) from CMSX-4 feedstock rods (Ross & Catherall Ltd. Sheffield, UK). Only the fraction of 45–105 μm was used for this work.

The system was equipped with a four-segment electron detector developed by Freemelt AB and in-house developed ELO imaging software. The build cycle for each layer was based on a regular PBF-EB cycle as depicted elsewhere [2]. After raking, a preheating step with a defocused electron beam was conducted to prevent powder smoke. After all subsequent melting steps had been finished an additional scan step for ELO image acquisition was added before the next powder spread by the rake. Hence, this modified PBF-EB cycle was identical to the cycle illustrated by Arnold et al. in [9].

The four-segment ELO detector was centred around the electron gun opening of the vacuum chamber at 165 mm above the build area. Therefore, the build direction BD is parallel to the z-axis and perpendicular to x-axis and y-axis in all ELO images presented in this study. An imaging area of 60 mm × 60 mm was scanned line per line with a scan line-distance $l_{off,ELO}$ of 0.10 mm, a beam power P_{ELO} of 60 W and a beam deflection velocity $v_{scan,ELO}$ of 10 m/s. The amplifier of the detector system operated at a sampling rate of 250 kHz. A python-based ELO imaging software was in-house developed specifically for image generation with the utilized four-segment detector. The ELO images were generated by logging the intensity signal of each detector segment to the corresponding beam position during the ELO scan. This was done for all detector segments individually as well as for combinations of detector segments. In addition, subtracting the individual imaging data of a pair of opposite detector segments was utilized for imaging the topography of the melt areas, whereas adding the imaging data of these two segments was utilized for imaging the material contrast. Furthermore, a mean image was generated by averaging the imaging data of all four detector segments.

For the build experiment a polycrystalline IN718 start plate with a diameter of 90 mm and a thickness of 22 mm was used. The build was started at a vacuum level of $< 5 \times 10^{-4}$ mbar and after the plate was heated to 1050 °C. Temperature measurement was done using a thermocouple attached to the bottom side of the start plate. Before each new powder rake, the build tank was lowered by 50 μm, whereas the powder tank was lifted by 150 μm. 9 cubes with 15×15 mm^2 layer surface and 25 mm of height were built. An inverted 45° pyramid with a height of 7 mm and an upper surface of 15×15 mm^2 was used as a connection between each sample and the start plate. Thin support pillars were molten around and in between the actual samples to support powder attachment to the plate in the first few millimetres of build height. Altogether, the given build experiment consisted of 640 layers of 50 μm height each. For all samples, snake hatching as well as a 90° rotation of the scan direction with each new layer was applied over the entire build height. Besides, no contouring was used in this work.

Process parameters were applied to each cube individually with beam power P_{melt} in the range of 300–488 W, hatch line distances $l_{off,melt}$ of 0.10 mm and 0.15 mm and beam deflection velocities $v_{scan,melt}$ of 400 mm/s and 750 mm/s. The parameter range was chosen from previous studies [5, 6] to ensure dense samples without surface uplifting, which may otherwise cause significant damage to the rake system and, therefore, require the premature stop of the experiment.
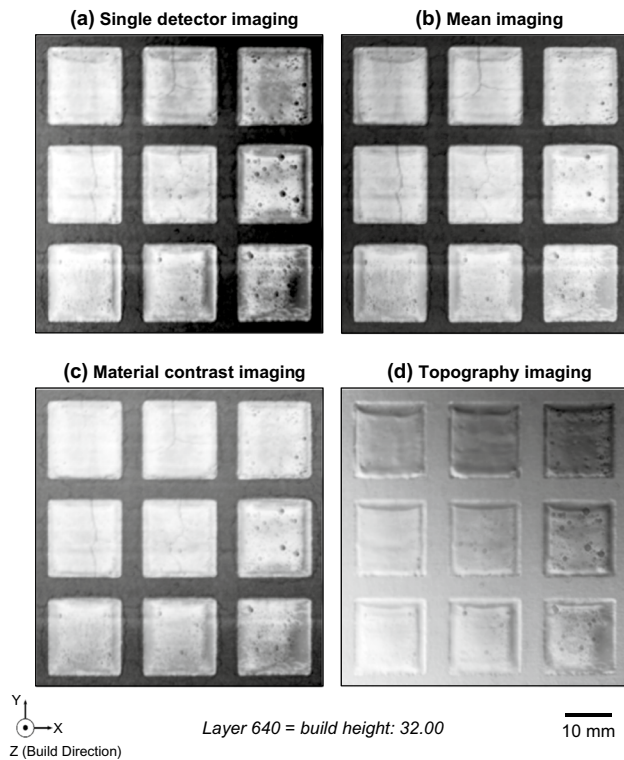
Fig. 1 Exemplary ELO imaging after 640 layers at a height position of 32 mm. The in-house developed ELO software enables four different imaging types: **a** images of individual detector segments, **b** mean imaging utilizing all four segments, **c** material contrast by adding the imaging data from two opposite detector segments and **d** topography by subtracting the data of the same two segments. Process parameters were taken from previous studies (P_{melt}: 300–488 W, $l_{off,melt}$: 0.15 mm or 0.10 mm with $v_{scan,melt}$: 400 mm/s or 750 mm/s, respectively) [5, 6]

3 Results and discussion

Layerwise ELO imaging of the entire PBF-EB experiment was successful despite the increasing metallization on all four detector segments. Figure 1 shows the upmost layer 640 at the final height position of 32 mm utilizing different imaging modes. Depending on the position of the detector segments, a pronounced brightness gradient in the generated images for individual (Fig. 1a) or two combined detector segments (Fig. 1c,) is observable. The dual detector ELO-experiments by Zhao et al. show a similar gradient in the image brightness of single detector imaging as well as the topographic imaging [18]. In the present experiment, only the mean image of all four detector segments (Fig. 1b) does not show this effect.

Figure 2 shows a close-up comparison of the surfaces of a cracked and a non-cracked sample using the four available ELO imaging types as well as their post-process counterparts. A surface-spanning crack on the sample surface (Fig. 2e) can also be identified in the single detector image (Fig. 2a) as

well as the mean image (Fig. 2b) and the material contrast image (Fig. 2c), yet not in the topography image (Fig. 2d). By comparison, the topography image is best suited for the depiction of surface features, such as uplifted centres and pits. Thus, the large black dots visible in the other three imaging types (Fig. 2a, b, c) can be identified as spherical foreign bodies lying on the previously molten surfaces. As indicated by the dashed circles, no pores or surface pits of equivalent size are present at the same positions on the sample surface (Fig. 2e) after freeing the samples from the sintered powder bed. A potential origin of these particles is sputtering during the melting step.

Figure 3 illustrates how layerwise ELO imaging can consequently be used for monitoring cracks in melt surfaces of CMSX-4 over process time. Figure 3a shows the ELO mean imaging of the last molten layer 640 at a height position of 32 mm after roughly 30 h of build time. Five out of nine melt areas (#1, 5, 6, 8, 9) show surface spanning cracks. The comparably long process time is caused by the extended heating time for each layer to balance the built temperature.

In Fig. 3b, the evolution of the temperature at the bottom of the start plate is plotted against the build time and the build height. After the build start at > 1050 °C, the build temperature was stabilized at about 1030 °C. The subsequent decrease by 2.6 °C per millimetre build height is likely caused by the increasing distance between the thermocouple and the molten surfaces. As indicated, all cracked samples in Fig. 3a were crack-free until at-least 16.50 mm of build height or, respectively, 15:14 h:min of build time.

Figure 3c exemplarily shows the appearance of surface cracking for sample #6 using close-ups of the generated mean images. The cracking was first observed at the height position of 20.00 mm (18:33 h:min, layer 400) and was already surface spanning yet poorly visible in comparison. Until 24.00 mm (22:18 h:min, layer 480) it becomes more pronounced with a cross-like appearance. This is most likely caused by increasing width of the crack. However, its cross-like shape is not present anymore in the ELO images at 30.00 mm build height (28:02 h:min, layer 600). It is also not present in the last ELO mean-image at 32 mm height (29:55 h:min, build end) as well as afterward on the sample surface. However, some ELO images of layers in between 30.00 mm and 32.00 mm of build height still show a more cross-like shape. Overall, the comparison of layerwise ELO-imaging and the sample surface indicates the presence of a large crack network inside the sample. In general, these surface-spanning cracks are in the middle of the melt surface and oriented parallel to the lateral direction. The discussion of the formation mechanism and the nature of theses cracks is beyond the scope of this study. However, in-situ ELO monitoring offers a practical approach to investigate the development of cracks during build process.
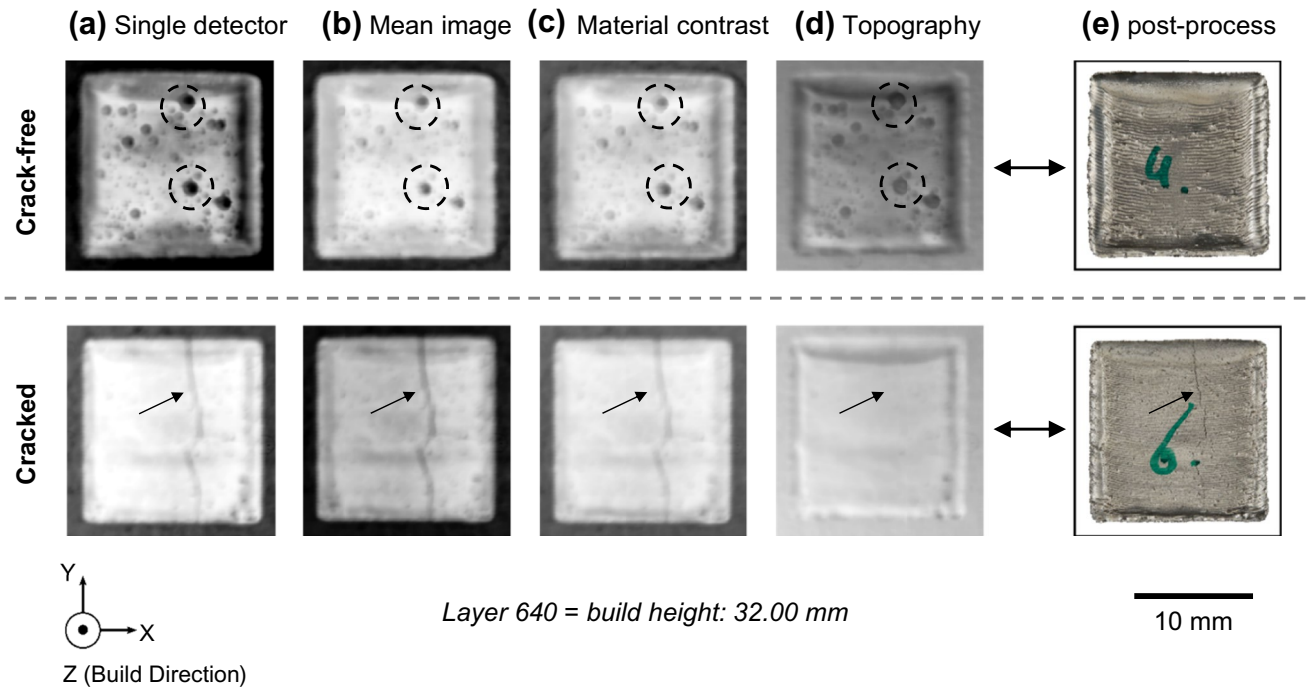
Fig. 2 ELO imaging of the last molten layer 640 (h: 32.00 mm after roughly 30 h build time) using different imaging types (**a**–**d**) compared to the respective sample surface after the build experiment (**e**). A crack-free sample (upper row: $P_{melt} = 390$ W, $l_{off,melt} = 150$ μm, $v_{scan,melt} = 400$ mm/s) and a cracked sample (lower row: $P_{melt} = 375$ W, $l_{off,melt} = 100$ μm, $v_{scan,melt} = 750$ mm/s) are depicted exemplarily. Particles on the surfaces are marked in ELO-images (dashed circles) of the crack-free melt area. Arrows in the lower row indicate the identical surface crack visible in the ELO-images and on the sample surface

4 Conclusions

A freely programmable PBF-EB system with an integrated four-segment ELO detector and in-house developed ELO imaging software was successfully applied for the in-situ crack monitoring during PBF-EB of CMSX-4. Comparing ELO imaging with the respective sample surfaces showed identical surface-spanning cracks. Using the layerwise monitoring allows to correlate crack initiation with the build height or the corresponding layer number. The conducted experiment clearly demonstrates the robustness and versatility of a four-segment ELO imaging system as a build quality control tool for PBF-EB.
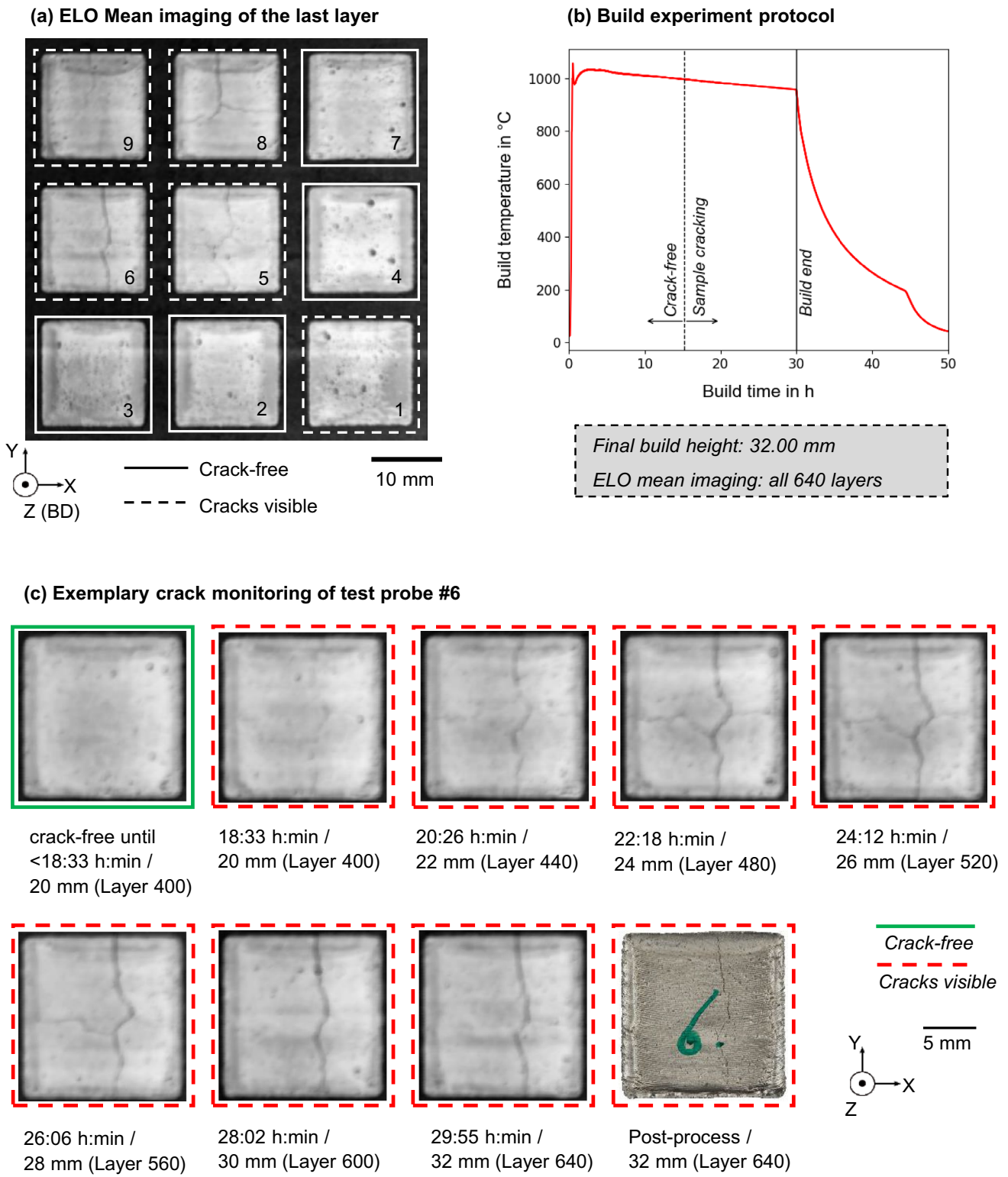
(a) ELO Mean imaging of the last layer

(b) Build experiment protocol

(c) Exemplary crack monitoring of test probe #6

Fig. 3 Monitoring of the conducted experiment utilizing ELO imaging: **a** Mean ELO imaging of the last molten layer shows five out of nine sample with surface spanning cracks (#1,5,6,8,9). **b** Temperature evolution at the start plate over process time. The time of the first crack observation is indicated. **c** Exemplary comparison of the mean ELO imaging of a cracked surface (#6) over build time and the corresponding build height and layer number. For all depicted surfaces the build direction is indicated by the z-axis, the beam deflection is parallel to the x-axis and the lateral direction is parallel to the y-axis

Declarations

Conflict of interest On behalf of all authors, the corresponding authors state that there is no conflict of interest.

References

1. Sames WJ, List FA, Pannala S et al (2016) The metallurgy and processing science of metal additive manufacturing. Int Mater Rev 61:315–360. https://doi.org/10.1080/09506608.2015.1116649
2. Körner C (2016) Additive manufacturing of metallic components by selective electron beam melting—a review. Int Mater Rev 61:361–377. https://doi.org/10.1080/09506608.2016.1176289
3. Harris K, Erickson GL, Sikkenga SL et al (1993) Development of two rhenium- containing superalloys for single- crystal blade and directionally solidified vane applications in advanced turbine engines. JMEP 2:481–487. https://doi.org/10.1007/BF02661730
4. Ramsperger M, Singer RF, Körner C (2016) Microstructure of the nickel-base superalloy cmsx-4 fabricated by selective electron beam melting. Metall and Mat Trans A 47:1469–1480. https://doi.org/10.1007/s11661-015-3300-y
5. Körner C, Ramsperger M, Meid C et al (2018) Microstructure and mechanical properties of cmsx-4 single crystals prepared by additive manufacturing. Metall and Mat Trans A 49:3781–3792. https://doi.org/10.1007/s11661-018-4762-5
6. Pistor J, Breuning C, Körner C (2021) A single crystal process window for electron beam powder bed fusion additive manufacturing of a cmsx-4 type ni-based superalloy. Materials 14:3785. https://doi.org/10.3390/ma14143785
7. Chauvet E, Tassin C, Blandin J-J et al (2018) Producing Ni-base superalloys single crystal by selective electron beam melting. Scripta Mater 152:15–19. https://doi.org/10.1016/j.scriptamat.2018.03.041
8. Sanchez S, Smith P, Xu Z et al (2021) Powder bed fusion of nickel-based superalloys: a review. Int J Mach Tools Manuf 165:103729. https://doi.org/10.1016/j.ijmachtools.2021.103729
9. Arnold C, Pobel C, Osmanlic F et al (2018) Layerwise monitoring of electron beam melting via backscatter electron detection. Rapid Prototyp J 24:1401–1406. https://doi.org/10.1108/RPJ-02-2018-0034
10. Price S, Lydon J, Cooper K et al. (2015) Temperature Measurements in Powder-Bed Electron Beam Additive Manufacturing. In: American Society of Mechanical Engineers Digital Collection
11. Dinwiddie RB, Dehoff RR, Lloyd PD et al. (2013) Thermographic in-situ process monitoring of the electron-beam melting technology used in additive manufacturing. In: Stockton GR, Colbert FP (eds) Thermosense: Thermal Infrared Applications XXXV. SPIE, 87050K
12. Grasso M (2021) In situ monitoring of powder bed fusion homogeneity in electron beam melting. Materials. https://doi.org/10.3390/ma14227015
13. Pobel CR, Arnold C, Osmanlic F et al (2019) Immediate development of processing windows for selective electron beam melting using layerwise monitoring via backscattered electron detection. Mater Lett 249:70–72. https://doi.org/10.1016/j.matlet.2019.03.048
14. Breuning C, Arnold C, Markl M et al (2021) A multivariate melt-pool stability criterion for fabrication of complex geometries in electron beam powder bed fusion. Addit Manuf 45:102051. https://doi.org/10.1016/j.addma.2021.102051
15. Arnold C, Breuning C, Körner C (2021) Electron-optical in situ imaging for the assessment of accuracy in electron beam powder bed fusion. Materials. https://doi.org/10.3390/ma14237240
16. Arnold C, Böhm J, Körner C et al (2019) In operando monitoring by analysis of backscattered electrons during electron beam melting. Adv Eng Mater. https://doi.org/10.1002/adem.201901102
17. Ledford C, Tung M, Rock C et al (2020) Real time monitoring of electron emissions during electron beam powder bed fusion for arbitrary geometries and toolpaths. Addit Manuf 34:101365. https://doi.org/10.1016/j.addma.2020.101365
18. Zhao DC, Lin F (2021) Dual-detector electronic monitoring of electron beam selective melting. J Mater Process Technol 289:116935. https://doi.org/10.1016/j.jmatprotec.2020.116935
19. Wong H, Neary D, Shahzad S et al (2019) Pilot investigation of feedback electronic image generation in electron beam melting and its potential for in-process monitoring. J Mater Process Technol 266:502–517. https://doi.org/10.1016/j.jmatprotec.2018.10.016
20. Grasso M, Remani A, Dickins A et al (2021) In-situ measurement and monitoring methods for metal powder bed fusion: an updated review. Meas Sci Technol 32:112001. https://doi.org/10.1088/1361-6501/ac0b6b
21. Fu Z, Körner C (2022) Actual state-of-the-art of electron beam powder bed fusion. European J Mater 2:54–117. https://doi.org/10.1080/26889277.2022.2040342
22. Freemelt AB (2021) FreemeltONE - official product brochure

Publisher's Note Springer Nature remains neutral with regard to jurisdictional claims in published maps and institutional affiliations.